



Study of Secondary Cosmic Rays and Astronomical X-Ray Sources using Small Stratospheric Balloons

Rupnath Sikdar, Sandip K. Chakrabarti, and Debashis Bhowmick

Indian Centre for Space Physics, 466, Barakhola, Singabari Road, Netai Nagar, Kolkata, 700099, West Bengal, India; rupnathsikdar1994@gmail.com

Received 2023 November 25; revised 2024 March 25; accepted 2024 April 19; published 2024 May 24

Abstract

The X-ray sources of the universe are extraterrestrial in nature which emit X-ray photons. The closest strong X-ray source is the Sun, which is followed by various compact sources such as neutron stars, black holes, the Crab pulsar, etc. In this paper, we analyze the data received from several low-cost lightweight meteorological balloon-borne missions launched by the Indian Centre for Space Physics. Our main interest is to study the variation of the vertical intensity of secondary cosmic rays, the detection of strong X-ray sources, and their spectra in the energy band of $\sim 10\text{--}80$ keV during the complete flights. Due to the lack of an onboard pointing system, low exposure time, achieving a maximum altitude of only ~ 42 km, and freely rotating the payload about its axis, we modeled the background radiation flux for the X-ray detector using physical assumptions. We also present the source detection method, observation of the pulsation of the Crab (~ 33 Hz), and spectra of some sources such as the quiet Sun and the Crab pulsar.

Key words: X-rays: stars – balloons – instrumentation: detectors

1. Introduction

The Indian Centre for Space Physics (ICSP) regularly launches light-weight balloons in its Dignity series of missions to study secondary cosmic rays and strong celestial X-ray sources (Chakrabarti et al. 2011, 2014, 2015, 2017; Sarkar et al. 2020; Sikdar et al. 2023b). Till now, one hundred and fourteen missions have been flown to the stratosphere at an altitude of 35–42 km.

Near the ground, below 2 km altitude, the dominant component emitting X-rays is due to the terrestrial radioactive elements (Tauchid & Grasty 2002). Secondary cosmic rays (CRs) are produced due to nuclear interactions of the atmospheric atoms with primary CR particles (Winckler 1961). The configuration of the magnetic field over the globe, its spatial distribution, and the interaction of the heliospheric magnetic field and geomagnetic field affect the intensity of primary CRs (Störmer 1956). The localized flux of planetary CRs can be disturbed by geomagnetic storms due to solar-charged particles and plasma-produced currents in the Earth's magnetic field. Thus, secondary CR flux may vary with solar activities (Usoskin et al. 2005; Sarkar et al. 2017; Utomo 2017). This varies with different latitudes, too (Ziegler 1996). In situ, procurement of atmospheric parameters and cosmic radiation data is usually carried out by modern radiosondes (Bazilevskaya & Svirzhevskaya 1998) on different platforms such as rockets, aircraft, and scientific balloon-borne missions (Bazilevskaya & Svirzhevskaya 1998; Fittock et al. 2011; Harrison et al. 2014; Chakrabarti et al. 2017). During the balloon-borne observations that are reported in this paper, the solar activities were very low, and thus our observed CR profiles remained the same on all the missions.

Results in this paper are obtained at the low-latitude region of about $\sim 14.5^\circ$ N, where the geomagnetic rigidity exceeds 10 GV and CR variation with latitude is minimal.

Along with the height variation of secondary CRs, which we measure in every flight, our goal is also to identify strong X-ray objects in the sky. The extraterrestrial astronomical sources in X-rays are mainly observed by satellites (RXTE, XMM-Newton, Chandra, Swift, Geostationary Operational Environmental Satellites [GOES], AstroSat, etc.) and also rocket missions and large balloon-borne experiments carried by big balloons (e.g., GRIP, PoGOLite, etc.). The novelty of ICSP's balloon missions is that we use very lightweight balloons and very low-mass payloads. Due to its lightweight, we could not afford to have any pointing system, and the payload box, including the detector, rotated freely and randomly in the sky at varying speeds, generally slowly at higher altitudes. Because of this, we are unable to observe a specific object for a long duration of time and cannot take the in situ background in each part of the sky. In fact, the on- and off-source data could not be taken from any specific source. To overcome these difficulties, we identify X-ray sources post-facto by first tagging each received photon with an accurate time stamp and checking if, after the model background subtraction as appropriate at the observational height, any R.A./decl. window of the sky has a significant signal-to-noise ratio. Modeling the background radiation is a little more involved. The radiation has two components: one is external and depends on local secondary CRs and solar activity, including geomagnetic storms, solar wind, etc. The second component is internal, which may come from the scattering of CRs with the detector, shielding, and

Table 1
General Information Related to the Specific Dignity (D) Missions

Missions	D92	D95	D100	D101	D102	D103	D113
Date	11.05.2016	14.05.2016	18.11.2016	19.11.2016	07.05.2017	08.05.2017	23.11.2019
Flight duration (h:m:s)	03:54:25	05:56:37	03:35:37	04:36:52	03:19:18	02:38:31	07:51:35 ^b
Lift Off (UT)(AM)	03:42:56	04:20:13	07:01:52	07:02:53	06:47:27	06:38:20	05:41:49
Launch Site ^a	23.65N, 87.72E	23.65N, 87.72E	23.71N, 86.95E	23.71N, 86.95E	23.65N, 87.72E	23.65N, 87.72E	23.65N, 87.72E
Landing Location	23.80N, 87.86E	23.78N, 86.59E	23.59N, 87.42E	23.39N, 88.23E	23.75N, 87.86E	23.49N, 88.08E	22.82N, 87.77E
Detector	Phoswich (5'')	Phoswich (5'')	Phoswich (5'')	Bicron 3M3/3	Phoswich (5'')	Phoswich (5'')	Phoswich (5'')
Collimator FOV ^c	6°	15°	12.8°	6°	15°	15°	15°
Maximum altitude (km)	41	40	41	41	39	39	42
Payload Tilt (degree)	6°	5°	15°	15°	0°	3°	0°

Notes.

^a All places are in West Bengal, India.

^b A long flight with a duration of approximately eight hours;

^c Field Of View.

collimator materials. Most of the detector background in the high-energy X-ray region is due to the internal radioactivity stimulated by CRs (Grieder 2001). To evaluate the background function at a particular balloon height above 30 km altitude, we have used the background models at various heights and extrapolated the background radiation at the observed heights.

In Section 2, we briefly describe the mission details we carried out. We present some results, such as the time variation of the balloon altitude and the light curves containing photon counts during these missions, in Section 3. Attitude measurement of the payload is described in Section 4, and calibration of the detector and energy resolution are described in Section 5. A comparison between the measured atmospheric parameters and the standard model is described in Section 6. The vertical variation of the CRs and its relation to ground radioactivity are presented in Sections 7 and 8. Details related to the background modeling are presented in Section 9. Detector and atmospheric responses are necessary to correct the detected source spectra, as shown in Section 10. The source detection method is discussed in Section 11. We also discuss the results of the Fourier transform and the detection of Crab pulsation frequency in Section 12. The spectrum of sources and the luminosity of Crab from the X-ray perspective are discussed in 13. A brief discussion on the limitations of our study is written in Section 14. Finally, in Section 15, we present our concluding remarks.

2. Mission Details

The philosophy, detailed theory, inspiration, and motivation behind the stratospheric balloon-borne missions are stated by Chakrabarti et al. (2014, 2017). Therefore, we present the details of the stratospheric balloon experiment in brief in this paper. First, we select the launching site, predict the landing locations using a web-based landing predictor such as the Cambridge University tool (Snowman et al. 2013) and the Geant4 simulation technique (Agostinelli et al. 2003), because the overall flight path depends mainly on wind conditions, the duration of the flight,

and the carrier balloon types. Our high-altitude balloon missions are lightweight (5–6 kg payload with a single plastic balloon carrier) and low-cost (~USD 600–1000 per flight). Our main goal is to concentrate on scanning the X-ray and gamma-ray skies. The payloads are compact and reusable after recovery. They are provided with a temperature shield using Styrofoam (thermal conductivity of only 0.03 W/m°C) due to pressure changes from ~1000 mbar (ground) to ~2 mbar (~42 km) during a mission. Typically, our scientific payloads remain at 10°C–15°C inside the box throughout a journey. For the payload carrier, we normally use Tata Institute of Fundamental Research (TIFR, Hyderabad, Andhra Pradesh, India)-made plastic balloons of thickness 5.7 microns and also commercially purchased rubber balloons with volumes of 4000 m³ and 1000 m³, respectively. The rubber balloon carriers require parachutes and are about 20–30 feet long when inflated. The length of a plastic balloon is around 100 feet. Balloons are filled with hydrogen gas with a density of ~0.0824 kg m⁻³ to achieve higher buoyancy in the atmosphere. The choice of a meteorological balloon carrier depends on the payload weight and parachute, if present. We have used three types of balloon configurations until now: one rubber balloon, two rubber balloons, and one plastic balloon for payloads weighing less than 2.5 kg, 3–5 kg, and 4–6 kg, respectively. Typically, a flight duration is 4–6 hr, but it takes about 3 hr for a single rubber balloon mission. The behavior of lifts in single and double balloon configurations is discussed in Chakrabarti et al. (2017) in detail. Here, all missions are plastic balloon carrier missions. General information about all the missions considered in this paper for data analysis purposes is provided in Table 1. The five main phases of launch, ascent, balloon burst, descent, and recovery of a mission operation are illustrated in Figure 1. The lower panel of Figure 1 shows a compact, Styrofoam-covered scientific payload and instruments inside the payload are discussed in Section 2.1.

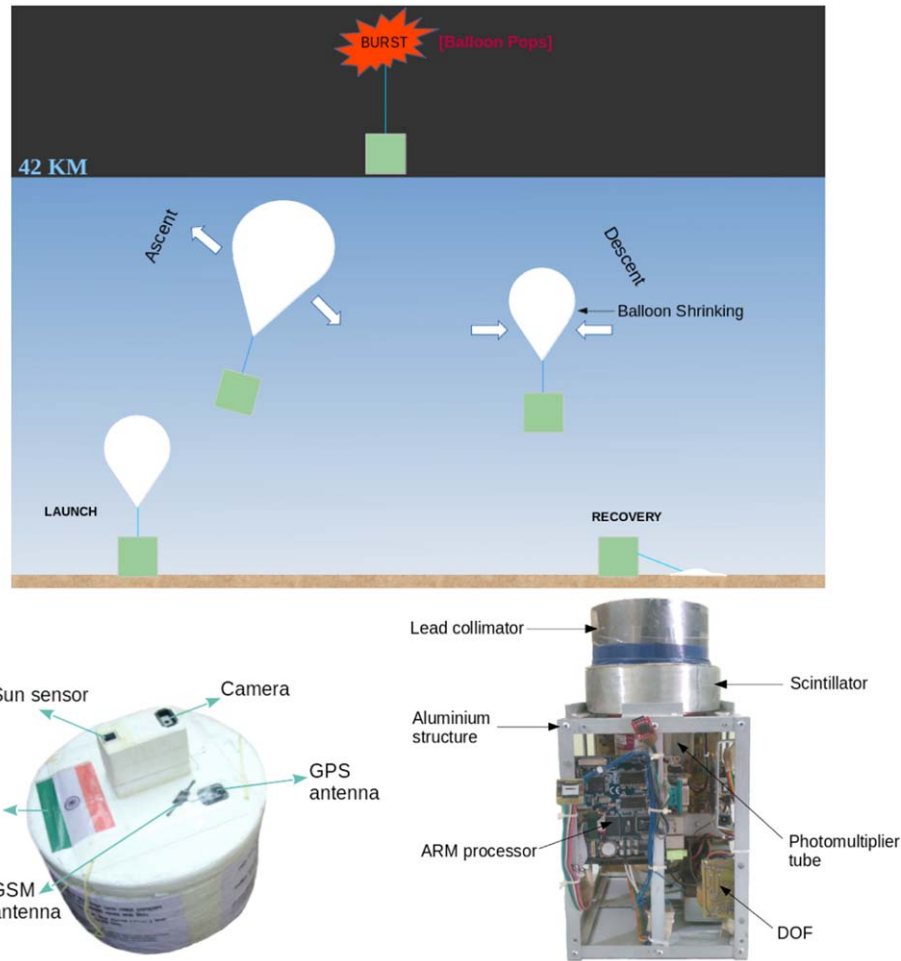


Figure 1. Upper: Various steps in a high-altitude plastic balloon mission operation. Lower left panel: A compact payload covered with thermocol for the balloon missions. Lower right panel: a typical payload instrument.

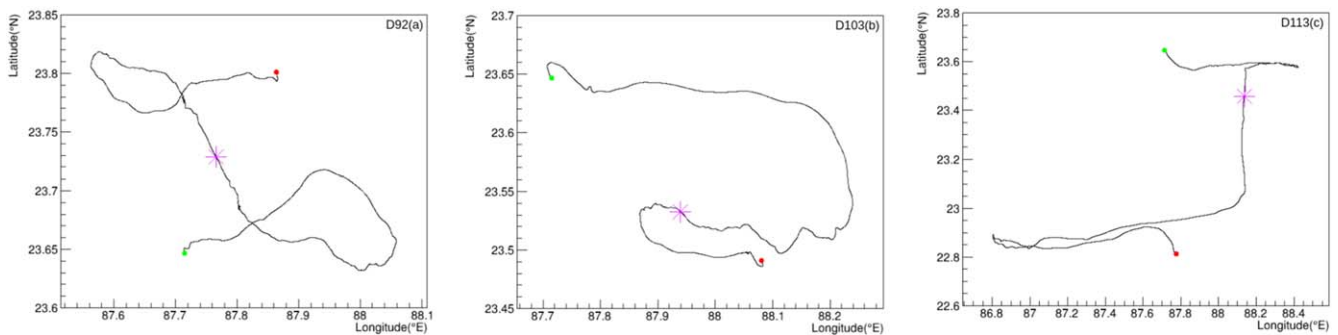


Figure 2. Horizontal displacements of the payload for missions D92, D103, and D113. Their burst locations are shown in violet. Green and red circles indicate the launching and landing sites, respectively.

The horizontal trajectories of the three flights with a single balloon as obtained from the GPS data are depicted in Figure 2. We observe that the excursions of the payload during the liftoff to the burst and from the burst to the landing do not cancel each other as the atmospheric parameters such as the pressure,

temperature, wind velocity and direction, the balloon burst time and altitude, ascent rate, and descent rate (which is affected by drag) are different. In mission D92, the horizontal displacements of the payload before the burst and after the burst are almost the same. However, in D103, the horizontal displacement before the

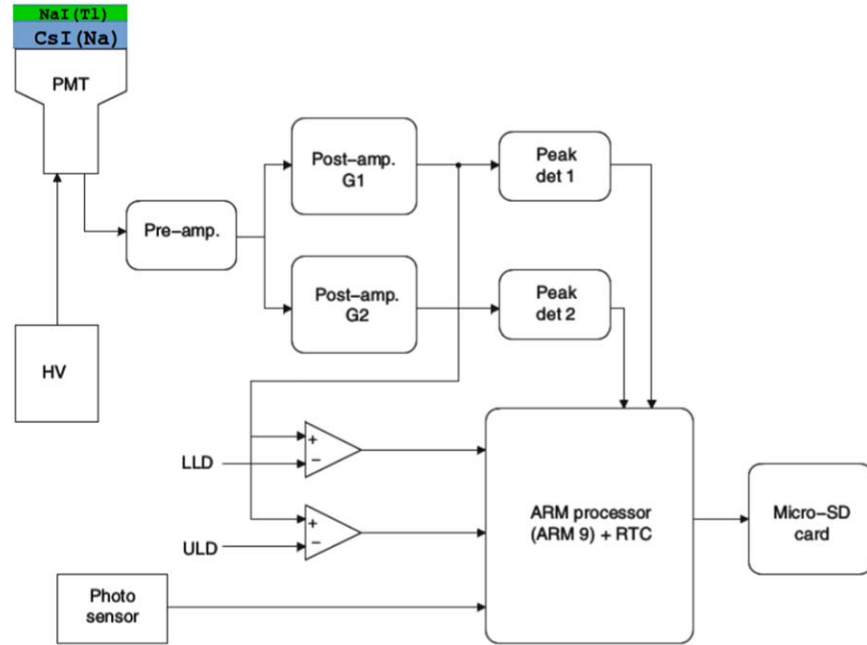


Figure 3. A block diagram of the balloon-borne experiment.

burst is greater than that after the burst. In D113, the trend is exactly the opposite.

2.1. Onboard Instruments

Our main device to detect X-ray and gamma-ray photons is a phoswich detector. This detector consists of two inorganic scintillation crystals, sodium iodide NaI(Tl) and cesium iodide CsI(Na). NaI(Tl) is placed over the top of the cesium iodide CsI (Na) due to the anticoincidence techniques, and together they are placed on a Photomultiplier Tube (PMT). To get a higher detector efficiency and reduce low-energy background noise, shielding the scintillator crystals with 1 mm thick tin and 0.2 mm copper at the underneath region is recommended. However, for our detector, we have used only lead shielding on the cylindrical surface of the detector to block 98% of the photons below 100 keV. We do not use any other shielding materials due to our weight restrictions. The specifications of this phoswich detector are as follows: 0.116 m diameter, 2.7 kg weight, and thickness of crystal materials NaI and CsI are 0.003 and 0.025 m of the same diameter respectively. The detector is fitted with a 0.5 mm-thick lead collimator. However, the collimator could not be used for measuring secondary CRs at energies above 100 keV in the atmosphere. If the field of view (FOV) is very large, then the collimator will permit a huge background (mainly CRs). Hence, we need to keep a suitable FOV value. The front-end instruments are the radiation detector and a high-voltage (HV) source, and the middle part of the instrument is a pre-amplifier and two post-amplifiers. Two post-amplifiers, G1 and G2, are used for the low energy range

of 15–150 keV (a gain factor of $0.16 \text{ keV channel}^{-1}$) and the high energy range of 100–2000 keV (a gain factor of $2.01 \text{ keV channel}^{-1}$), respectively. For payload attitude measurement purposes, we use the 9DOF data, which contain a 3-axis accelerometer, a 3-axis magnetometer, and a 3-axis gyroscope. Details of the instrument readout process, device operations, data storage, and their purposes are explained in detail in Chakrabarti et al. (2017), Bhowmick et al. (2019). Other ancillary equipment is the GPS/GSM tracker to give the positions of the payload, the atmospheric pressure and temperature sensors, one or more video cameras for viewing the horizon, the balloon, and the Earth’s surface, etc. The block diagram of the total experimental setup is shown in Figure 3. At very low energy, below $\sim 10 \text{ keV}$, the background noise is high. So, in data analysis, we avoid the lower energy component until 10 keV due to the noise from the detector. With the presence of the absorption line at 88 keV and effectively blocking up to 80 keV by the collimator, high-energy photons passing through the detector crystal and also the deposition of their energy producing new partial counts using Compton scattering and pair production, we choose photons with energy up to 80 keV. At high energies, above $\sim 100 \text{ keV}$, the lead collimators are transparent, and thus photons enter the detectors from all directions. Therefore, we do not take any photons with energies above 100 keV.

3. Light Curves from Our Missions

The plot of the detector count rates versus payload altitude (or time) for the entire mission gives us a light curve. Figure 4

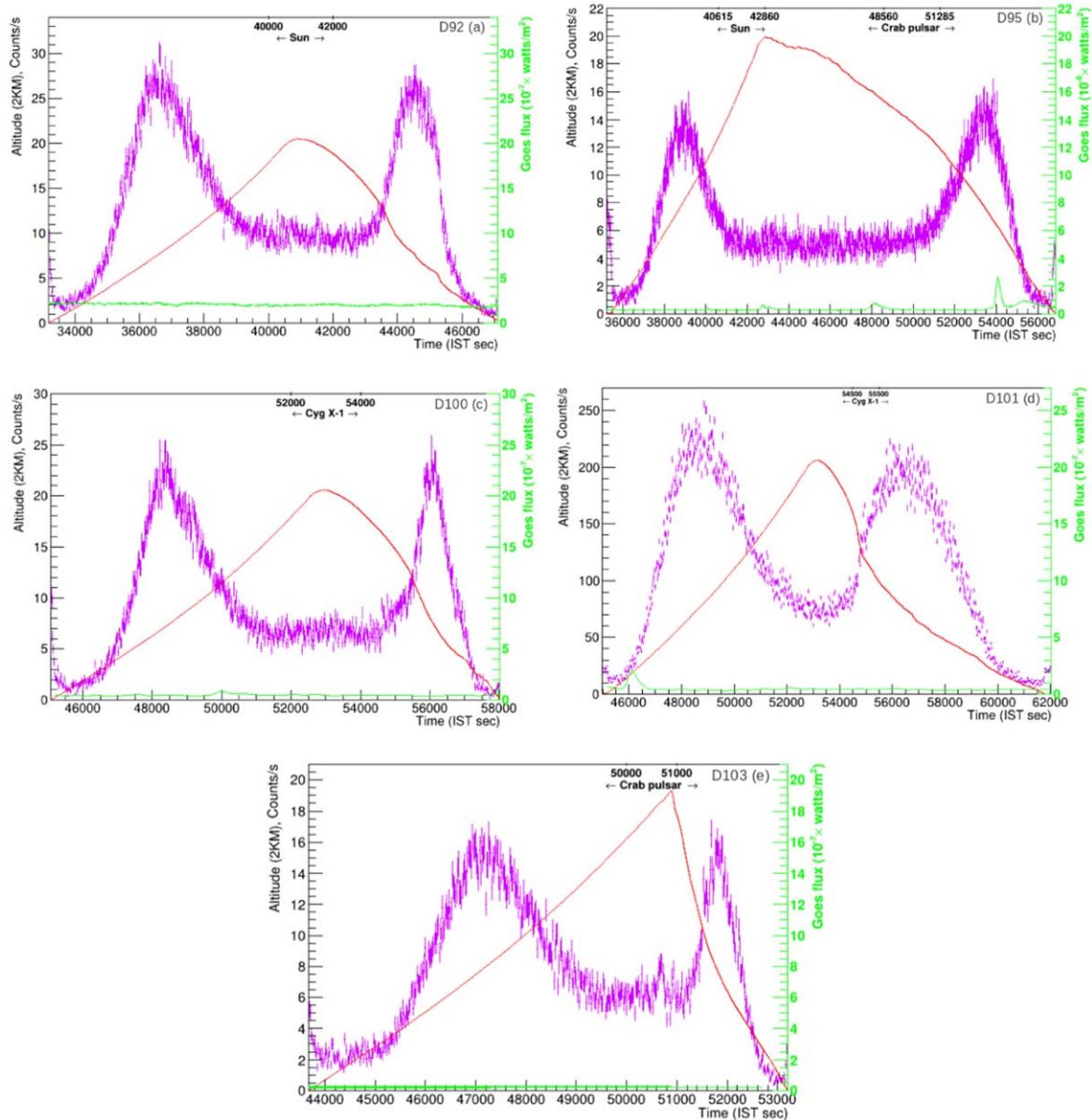


Figure 4. Light curve (magenta) of the entire mission in the energy range (20–65) keV, payload altitude (red), and GOES X-ray solar flux (green) for (a) D92, (b) D95, (c) D100, (d) D101, and (e) D103 missions. Regions of strong X-ray sources are also marked in each panel.

gives the light curves of the specified missions. For light curves, we take a 20 s time bin in the energy range of 20–65 keV and superpose the GOES satellite X-ray flux data and payload altitude profile of the missions. Regions of the strongly known X-ray objects that could be within our FOV in each of the missions are marked in Figure 4. Whether these sources are detected depends on the duration for which our detector was pointing at them during the mission and the significance of the detection.

As the payload is launched, we receive a few photons from terrestrial radioactive sources such as ^{238}U , ^{232}Th , ^{226}Ra , etc. in

the ground. Photon flux from the terrestrial radioactive elements would be different in different geographic locations (Zhang et al. 2004) due to different distributions of radioactive elements. At altitudes between 1 and 2 km, the secondary CRs start to dominate over the rate from ground radioactivity, which are generated by the nuclear interactions of primary CRs with the most abundant atoms and molecules in the atmosphere, such as nitrogen, oxygen, etc. With increasing altitude in the atmosphere, this secondary cosmic radiation intensity increases (Harrison et al. 2014). Secondary CRs are mainly subatomic particles and high-energy photons and are most intense in the

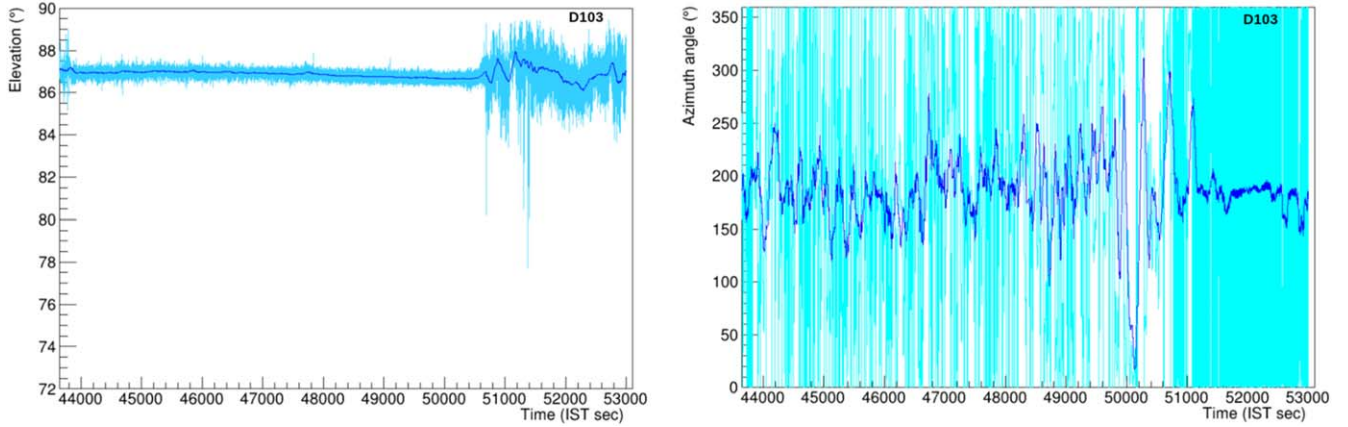


Figure 5. The elevation (azure) profile is shown in the left panel, and the azimuth (cyan) profile is shown in the right panel for the D103 mission with the running average (blue).

height range of 15–20 km from Earth’s surface in the stratosphere region, depending on the latitude and solar activity. This height is called the Regener-Pfotzer maximum (R-P maximum) (Carlson & Watson 2014; Sarkar et al. 2017). This can be seen to be present in all the light curves in each panel of Figure 4. R-P maximum has a maximum muon neutrino flux (Gaisser 1990), and other ion pairs vary with solar activity (Sarkar et al. 2017), geomagnetic latitude (Ziegler 1996; Saraiva et al. 2020), geomagnetic storms (Phillips et al. 2016), etc.

We generally see that the detector count rate decreases with increasing height above the R-P maximum until about 35 km, and after that height, the light curve shows a broad peak or a collection of short peaks if X-ray sources are present from 35 km to burst height. In the D95 and D101 missions, Class B and C-level solar flares are present during the mission execution. Because of the formation of holes at the balloon surface during the burst time by external forces or an imbalance of air density between the inside and outside of the balloon, the altitude at 45,000 s, IST, is bumpy in the landing phase in the altitude profile of D95. In D103, a dent at around 50.5 ks, IST, in the light curve could be disturbances caused by the rupture of the balloon during the burst, as confirmed by the altitude measurement and onboard installed camera footage. In D101, the radiation intensity is approximately ten times higher in comparison to the other missions. This is because we used a 3-inch bicon detector, which has very different quantum efficiency, effective area, etc.

4. Payload Attitude Measurement

To obtain the attitude data for each photon received onboard, we use the 9DOF Inertial Measurement Unit (IMU), namely, the accelerometer, magnetometer, and gyroscope sensors. Details of the payload attitude calculation are given below. We measure the proper attitude in the horizontal coordinate system (elevation and azimuth angle) of the payload, which is

calculated using IMU sensor onboard data. First, we calculate the roll, pitch, and yaw angles from the equations as given below (Ozygcilar 2015).

$$\tan(\phi) = G_y/G_z, \quad (1)$$

$$\tan(\theta) = -G_x/(G_y \sin \phi + G_z \cos \phi), \quad (2)$$

$$\tan(\psi) = \frac{B_z \sin \phi - B_y \cos \phi}{B_x \cos \theta + B_y \sin \theta \sin \phi + B_z \sin \theta \cos \phi}, \quad (3)$$

where ϕ , θ , and ψ refer to the roll, pitch, and yaw angles, respectively. G_s are the accelerometer readings, and B_s are the magnetometer readings along the three axes. Though the above three equations have an infinite number of solutions at multiples of 360° , it is the convention to restrict the solutions of roll, pitch, and yaw between -180° and 180° . A constraint is again imposed on the pitch angle, only to limit it to the range of $(0-90 \text{ deg})$, which ensures that only one unique solution (pitch and roll angles) exists for the particular orientation of the device. Finally, we estimate the elevation and azimuth angles of any detector direction depending on the IMU orientation during the entire mission. In Figure 5, note that the elevation angle is nearly the same throughout mission D103. The azimuth plot shows that the payload was continuously rotating between the angles of 0° and 360° from launch to landing. Thick lines show the running average.

5. Detector Properties

We use a two-layer, namely, NaI(Tl) and CsI(Na) scintillator-based phoswich detector that detects X-rays, gamma-rays, as well as alpha, beta, etc. For calibration and energy resolution purposes, we use a few laboratory radioactive isotopes: ^{241}Am , ^{133}Ba , and ^{152}Eu . Energy lines at 39.5 and 121.9 keV for Eu, 30.9 and 81.0 keV for Ba, and 59.5 keV for Am are plotted and fitted with channels that follow a straight line $E = mX + c$, where $m = \text{slope}$ and $c = \text{constant}$. This will give us the correlation between the incident count energy (E) and channel

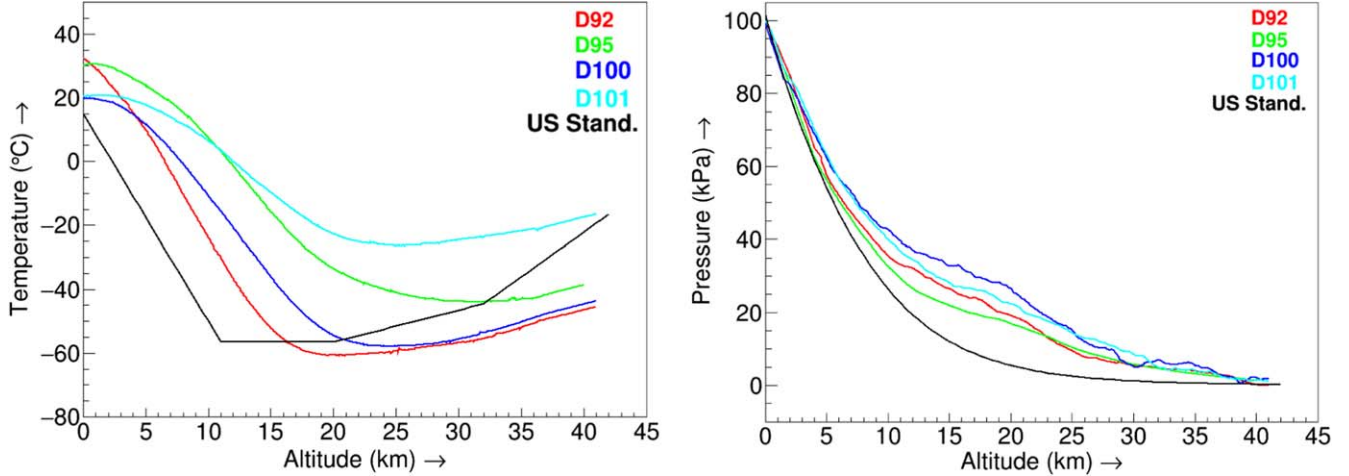


Figure 6. (left) US standard atmospheric profile superimposed on the temperature plot of four missions (D92, D95, D100, and D101). (right) Pressure profile of missions D92, D95, D100, and D101 with US standard modeling pressure data. The color of each curve is seen from the mission name given in the upper right corner of both diagrams.

number (X) from 1 to 1024. Resolution at every energy level requires one to analyze the energy spectrum of a multichannel pulse analyzer for the detector. The equation of the detector resolution varies with energy as aE^{-b} , where a and b are constants. For example, corresponding to channel 300, the energy is 48 keV and the resolution is 0.25.

6. Atmospheric Parameters

Two physical parameters, such as temperature and pressure, will vary with the payload altitudes and latitudes of the geographic coordinate system. The measurement sensors for such parameters of our balloon mission are discussed in detail in Chakrabarti et al. (2017). Here, we discuss the data from four missions to study the change in temperature and pressure with height from the Earth's ground. For the summer, we choose D92 and D95, while for the winter, we choose D100 and D101. In Figure 6 (left side), we superpose the temperature profiles of our four missions with temperature profiles according to the US standard atmosphere model 1976. We see temperature (T) decreases with increasing altitude in the troposphere until the tropopause, and in the stratosphere, T remains almost constant between the heights of 10 and 20 km. The difference in ground temperature from the standard U.S. model is due to the ground temperature at the launch site in India. The pressure profile of such missions, along with those from the US standard model, is shown on the right side in Figure 6. In that figure, the maximum pressure deviation from the standard model appears in the region of the R-P maximum position, possibly due to the high-intensity radiation effect on the pressure sensor of piezoresistive material (Chakrabarti et al. 2017), and has the least deviation at the initial and highest altitudes. The colors of the particular missions are as in the text.

7. Ground Radioactivity and Secondary Cosmic Rays

The radiation intensity of the terrestrial radioactivity at the ground (assumed to have an altitude of 0 km, i.e., the mean sea level) decays sharply according to the empirical relation $K[1 - h/\sqrt{(h^2 + a^2)}]$ with altitude (h), where K and a are the initial photon flux and the detector's radius covering an effective circular area by assuming to take only the vertically arriving counts and not other projected photons on the detector due to the high absorption rate of the atmosphere. In Figure 7, this empirical function is drawn from the altitude of 0 to 8 kilometer with the running average of the light curve. The values of parameters K and a are ~ 7.55 counts/s and ~ 2.15 km respectively for mission D95.

In the Earth's atmosphere, the induced ionization is proportional to the intensity of the Galactic cosmic radiation (Stozhkov et al. 2002). Here, secondary CRs (counts s^{-1}) follow the equation $Ae^{Bh} \times (h - C)^2$ between the altitudes 1 and 15 km, where A ($\sim 57.33 \times 10^{-3}$ counts $s^{-1} km^{-2}$) stands for the normalizing constant depending on the maximum CR flux, i.e., the R-P maximum recorded on the mission date, while B ($\sim 1.93 \times 10^{-3} km^{-1}$) and C ($\sim 30.91 \times 10^{-2} km$) are constant parameters. This result is analogous to the model of Usoskin-Kovaltsov (Usoskin & Kovaltsov 2006).

8. Vertical Variation of Secondary Cosmic Rays in the Atmosphere

Secondary CRs in vertically upward ($\cos \theta \approx 1$) and downward ($\cos \theta \approx -1$) directions are produced by the nuclear interactions of atomic particles in the atmosphere with the primary CRs, as we already wrote in Section 3. Theta represents the zenith angle. The left panel of Figure 8 displays the normalized secondary CR counts (counts s^{-1}) with a bin

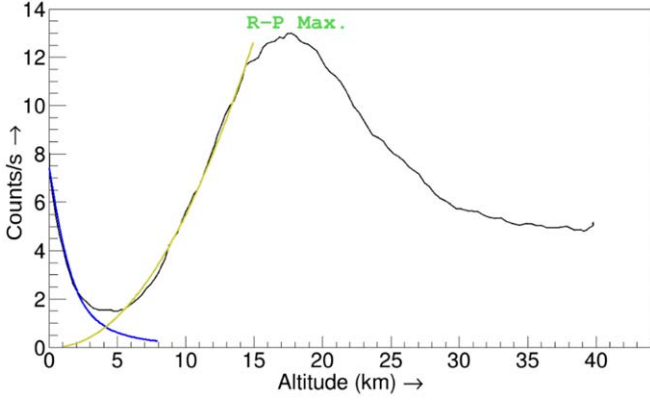


Figure 7. Two curves, one for the radioactivity (blue) and the other for the atmospheric cosmic radiation variation (yellow) with altitude, are superimposed on the running average light curve of D95 during ascent.

width of 800 m for several missions, and the right panel features the average in situ measured count rate without error bar from 1 km onwards due to radioactivity on the ground. The minimum photon counts due to CRs at about 1 km above the ground remain more or less the same for all the missions (as is evident on the left side in Figure 8), which we take as the normalization, and the normalization process with details is stated in Sarkar et al. (2017). The peaks in Figure 8 represent the R-P maxima, where the leptonic and hadronic components of the cascade are the most intensive (Gaisser 1990), and they vary with solar activity and geomagnetic latitude (Ziegler 1996; Usoskin et al. 2005; Sarkar et al. 2017; Sikdar et al. 2023a). In the atmosphere, the secondary cosmic radiation is a function of altitude (here, we take h in km) depending on the atmospheric density, and the ionization cross section is proportional to the square of h (Stozhkov et al. 2002). Equation (4) of the secondary CR flux at a particular altitude in the atmosphere has been written as follows

$$I_r(h) = A_n \times e^{-Hh} \times (h - h_0)^2, \quad (4)$$

where A_n is the normalizing constant depending upon the detector properties, the exponential term implies the air density with a constant factor H , which is a function of temperature lapse rate, and h_0 simply indicates a constant parameter. Suitable values of the parameters A_n , H , and h_0 of the function I_r are $2.43 \text{ counts s}^{-1} \text{ km}^{-2}$, 0.19 km^{-1} , and 4.74 km , respectively. This function is plotted over the mean secondary CR diagram in Figure 9. The deviation between the function I_r and the measured value at 6 km is due to the combination of ground radioactivity with the secondary CR flux. At 31 km, the deviation is due to the presence of X-ray sources in space.

9. Modeling of Detector Background

External background radiations are the incoming counts consisting of downward and upward secondary CRs, mainly gamma photons (Sarkar et al. 2019). Internal radiation may be

produced by gamma-ray scattering with detector crystals, Compton scattering, pair production, photons escaping due to annihilation, (Peterson et al. 1972) etc. For the calculation of the background counts where sources are within FOV, we faced some difficulties due to the lack of an onboard pointing system, the fact that the payload freely rotates in the sky, etc. Therefore, we have to model background radiation, which is based on our previous empirical model discussed in Sarkar et al. (2019). The background model present in Sarkar et al. (2019) is used in the Sikdar et al. (2023c) work and is also verified by the detailed calculations presented in Sarkar et al. (2020) and Sikdar et al. (2023a). We considered the detector background spectral range from altitude 20 to 30 km in each atmospheric layer of 1 km as normal backgrounds, as stated in Sarkar et al. (2019). The background radiation $N(h_{\text{ad}}, E)$ is a function of energy (E) and vertical height in terms of the atmospheric depth (h_{ad}), according to the following equation

$$N(h_{\text{ad}}, E) = \sum_{i=0}^n P_i(h_{\text{ad}}) E^i \text{ counts s}^{-1} \text{ keV}^{-1}, \quad (5)$$

where $P_i(h_{\text{ad}})$, which is the coefficient of E^i , varies with atmospheric depths and depends on the geomagnetic latitude of the experiment and solar activity. The i stands for the summation index of the lower limit of value zero. We found that this background equation is a ninth order polynomial ($n = 9$) for missions D92 and D103.

In the detector spectrum, there are several internal lines and low background noise at 10 keV, at (25–30) keV due to K-line X-rays from the spallation of tellurium (Thompson 1974; Gruber et al. 1996) and due to the natural radioactive source ^{125}I at ~ 68 keV for mission D92 in Figure 10 (left side). In the detector background spectrum for mission D103, the energy lines are due to low background noise at ~ 12 keV, due to natural radioactive sources ^{210}Pb at ~ 42 keV, and ^{125}I at ~ 68 keV, as clearly presented on the right side in Figure 10. The variation of low-energy background noise is varied exponentially, and other lines are Gaussian with energies for several atmospheric depths (Sarkar et al. 2020; Sikdar et al. 2023a).

We fitted the detector background using Equation (5) and extracted the model parameters (P_i) for different atmospheric depths and then fitted their variations. We found that P_i varies linearly with atmospheric depths. In Figure 10, we show the comparison of the detector background and modeled background for missions D92 at an altitude of 30 km and D103 at 20 km. Using these parameters, we are able to calculate the background at higher altitudes where the Sun and Crab pulsar are inside the detector FOV.

10. Detector and Atmospheric Responses

The detector response matrix function and ancillary response (change in effective area for different energies) are computed

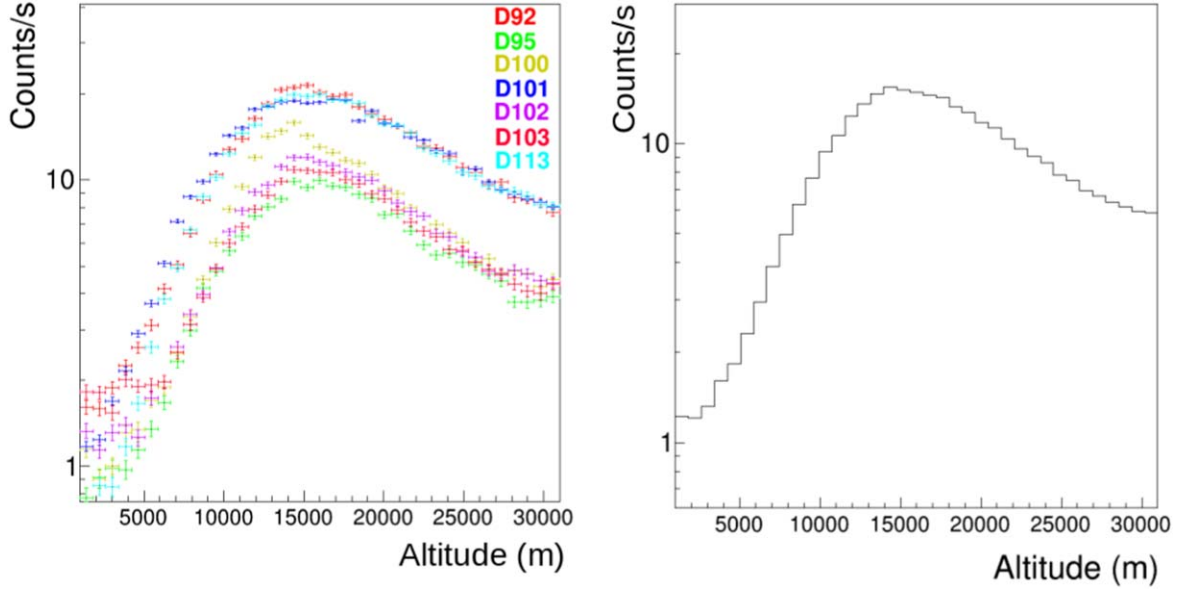


Figure 8. (left side) Cosmic radiation as a function of the detector altitude for the missions D92 (red), D95 (green), D100 (yellow), D101 (blue), D102 (violet), D103 (pink), and D113 (cyan); (right side) average CR flux variation with respect to altitude.

using the Geant4 simulation technique for the same detector, discussed in detail in Sarkar et al. (2019). Apart from this, from the sensitivity calculation (Sarkar et al. 2019), we can say that strong X-ray sources such as the Crab pulsar and the Sun are detected in our detector. To eliminate the residual atmospheric absorption of the X-ray radiation coming from astronomical sources, we have to calculate the atmospheric response. For this, we consider the NRLMSISE-00 standard atmospheric model (Picone et al. 2002) to construct the geometry of the atmosphere. The calculation of atmospheric response for different altitudes in the photon energy range of 10–100 keV is already done using the Geant4 simulation toolkit by Sarkar et al. (2019).

11. Source Detection Process and Missions Data Analysis

We used the sky scanning method since we have no automatic pointing system to observe X-ray objects. In such a method, we need to transform the horizontal (Earth) into an equatorial (celestial) coordinate system for every detected photon, as elaborated on in Section 11.1. The analysis of data from missions D92 and D103 for source detection purposes is in Section 11.2.

11.1. Coordinate Transformation

The conversion of horizontal coordinates (elevation and azimuth) into equatorial coordinates (RA and DEC) is done in

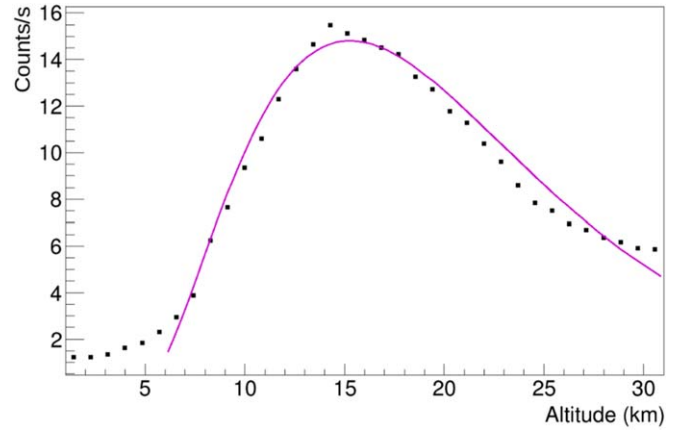


Figure 9. Black squares are the measured average cosmic flux at various altitudes and the function I_r (magenta) is superimposed.

the following way:

$$\sin(\delta) = \sin(a)\sin(\phi) + \cos(a)\cos(\phi)\cos(z), \quad (6)$$

$$\cos(H) = \frac{\sin(a) - \sin(\phi)\sin(\delta)}{\cos(\phi)\cos(\delta)}, \quad (7)$$

$$\text{RA} = \text{LST} - \frac{H}{15}, \quad (8)$$

where H is the hour angle, LST is the local sidereal time, ϕ is the observer's geographical latitude, a and z are the elevation

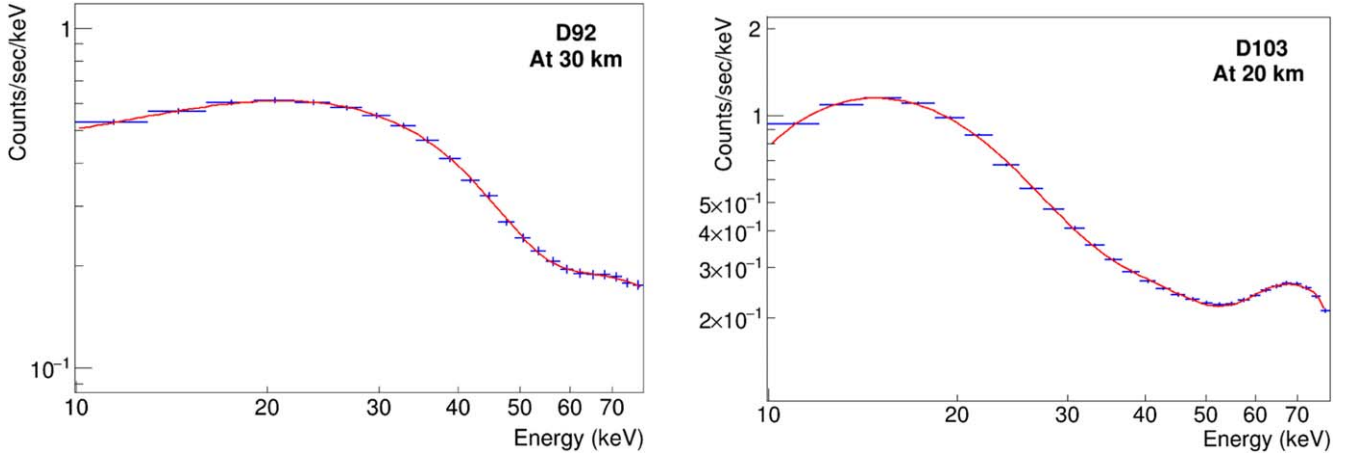


Figure 10. Detector background spectrum (blue) and model background function (red) for missions D92 at 30 km (left) and D103 at 20 km (right).

and azimuth angles, and δ and R.A. are the decl. and R.A., respectively.

11.2. Missions D92 and D103

The detection of the Sun in D92 and the Crab in D103 is already presented in the paper Sikdar et al. (2023c). However, the case of detection would be stronger if we can demonstrate that we continue to detect the sources in an unbiased way at all altitudes. We show this using the new background model. The result agrees with our previous results. We use the SIMBAD (Wenger et al. 2000) or NED (Mazzarella 2007) astronomical databases to find X-ray astronomical objects in our scanned area. The 2D histograms with the filling of raw counts (source counts plus background counts), exposure time, background counts, source counts after background subtraction, and source count rate, which is modified by atmospheric effects, for missions D92 and D103 are depicted in Figures 11, 12, 13, and 14. We get a higher count rate, i.e., deeper color in the fifth histogram at the location of the source in the R.A. and decl. bins. Therefore, the intensity of photons from the bin containing the source is at its maximum, as expected. In each figure, sources are to be found in the phoswich data in the energy range of 20–65 keV and the signal-to-noise ratio, i.e., the ratio of source counts and standard deviation of background counts, which is the square root of the background counts according to the Gaussian or Poisson distribution, greater than 3. This corresponds to the 99.99% confidence level for detection. We break up the R.A.-decl. plane into several box bins. The size of the bins was chosen to have a signal-to-noise ratio better than the 3σ level. This is found only after ascertaining the amount of time the detector spent in those R.A.-decl. bins and dividing the total number of photons by the time spent in each bin.

12. Timing Properties of the Crab Pulsar

The timing properties of the Crab were already discussed in Sikdar et al. (2023c). Here, we also provide a detailed analysis of such properties using the data from mission D103. We take the raw data from an altitude range of 36–38 km. We use 1 ms binning of 20–70 keV photons and draw the light curve shown in Figure 15. Figure 15 (upper panel) displays several 6 s chunks of data, followed by 1 s gaps during the data writing process. Figure 15 (middle panel) depicts the R.A./decl. of all the binned photons received in each of the six-second chunks of data. The Crab’s location is shown by two black lines drawn at the Crab’s R.A. and decl. We identify several chunks of data obtained from the region of the sky close to the coordinates of the Crab. Out of these, small segments are less than one second, slightly more than two seconds, and less than one second from three chunks of data (50531–50537) s, (50566–50572) s, and (50769–50775) s within the detector FOV (6 deg in the mission under consideration), as indicated in Figure 15 (lower panel). We reject the data chunks taken in (50531–50537) s and (50769–50775) s due to the very short exposure of the Crab. Therefore, we used the 2 s data of the 50,566–50,568 s duration. This is the selection process of data for taking the Fourier transform of the light curves of our detected source, Crab, to see whether there are any intrinsic pulsations. Not surprisingly, we indeed found the presence of the 33 Hz pulsation in these data.

For frequency calculation using the fast Fourier transformation, we relied on the web-based Lomb-Scargle algorithm (Akeson et al. 2013) which showed its highest peak at ~ 33.22 Hz, as depicted in the left panel of Figure 16. The right panel of Figure 16 gives the phase plot, clearly showing the two significant peaks separated by about 0.4 in phase (Jain & Paul 2011).

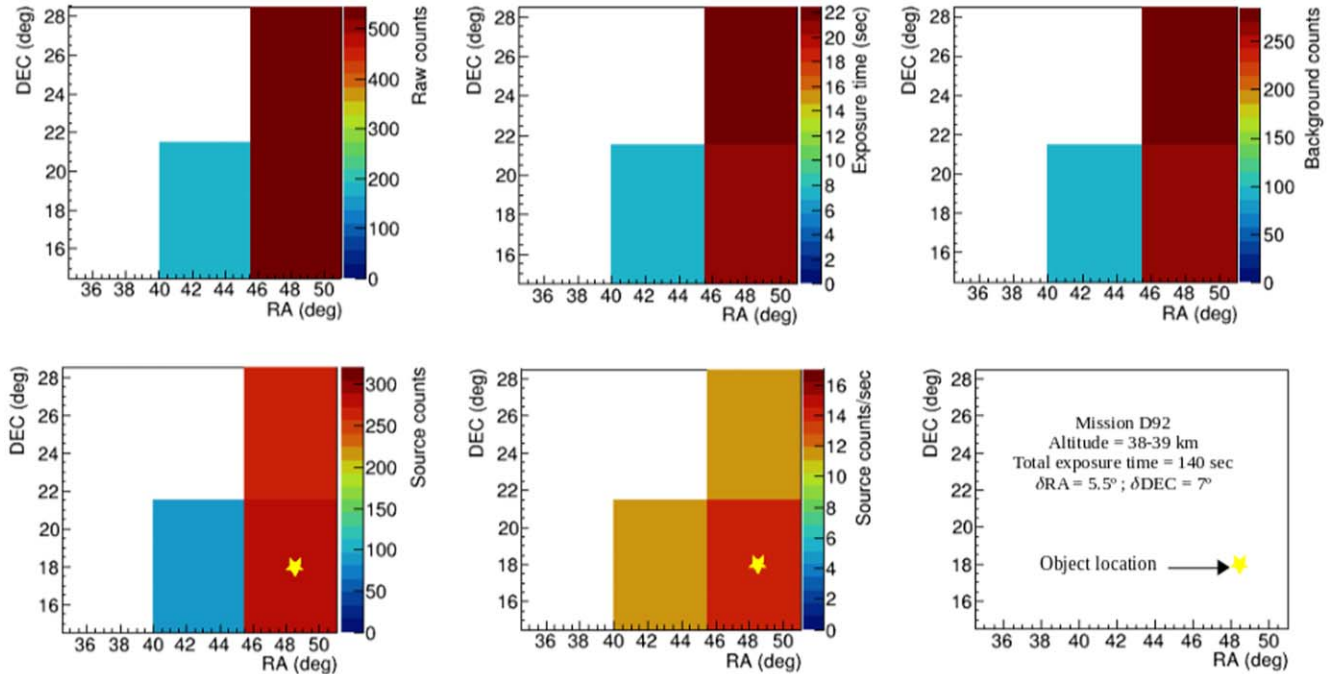


Figure 11. Different phases for the source detection in mission D92. The Sun is only detected at 38 km.

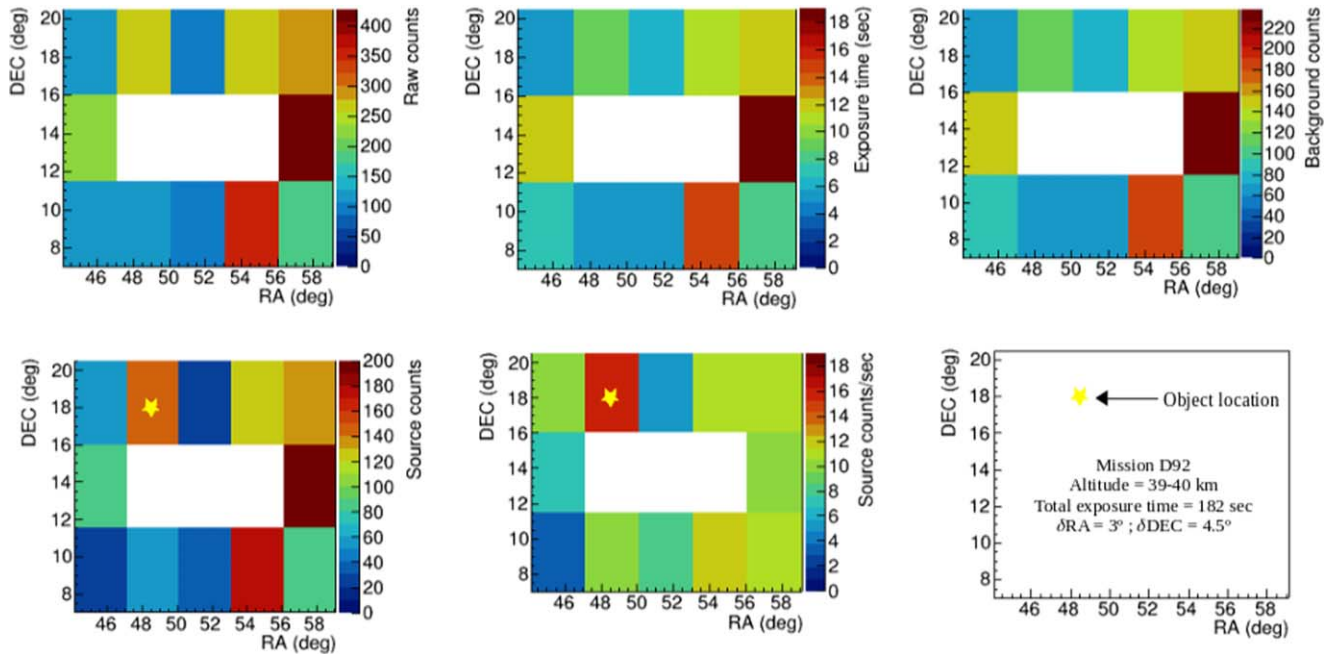


Figure 12. Different phases for the source detection in mission D92. The Sun is also detected at 39 km.

13. Spectral Analysis of the Sun and the Crab

The spectrum of the Sun in the quiet state is presented in the paper Sikdar et al. (2023c) and that of the Crab pulsar in Sarkar et al. (2019). Here, we compute the solar spectrum using the new background model, which also agrees with the result in

Sikdar et al. (2023c). We also include the Crab spectrum. The parameters obtained from the Crab spectral fit from our present fit are similar to our previous results presented in Sarkar et al. (2019). The spectra of the Sun and the Crab pulsar are plotted in the energy ranges of (20–50) keV and (20–65) keV,

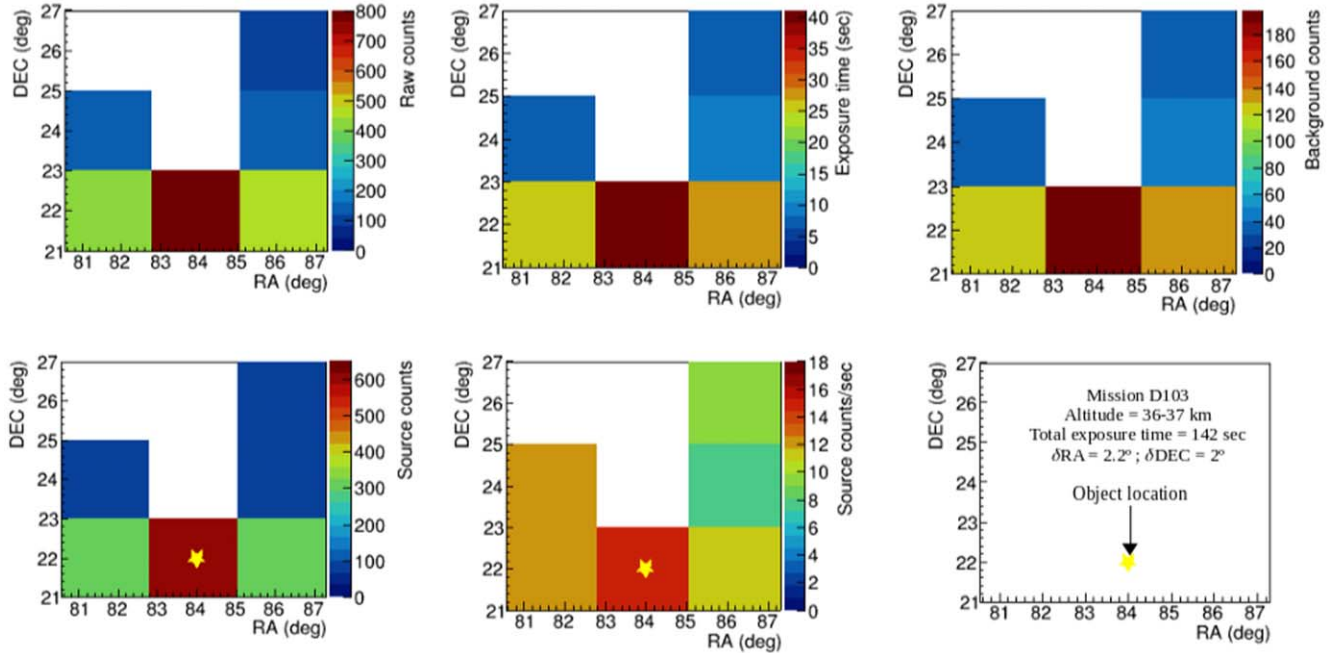


Figure 13. Different stages for the source detection in mission D103. The Crab pulsar is only detected at 36 km.

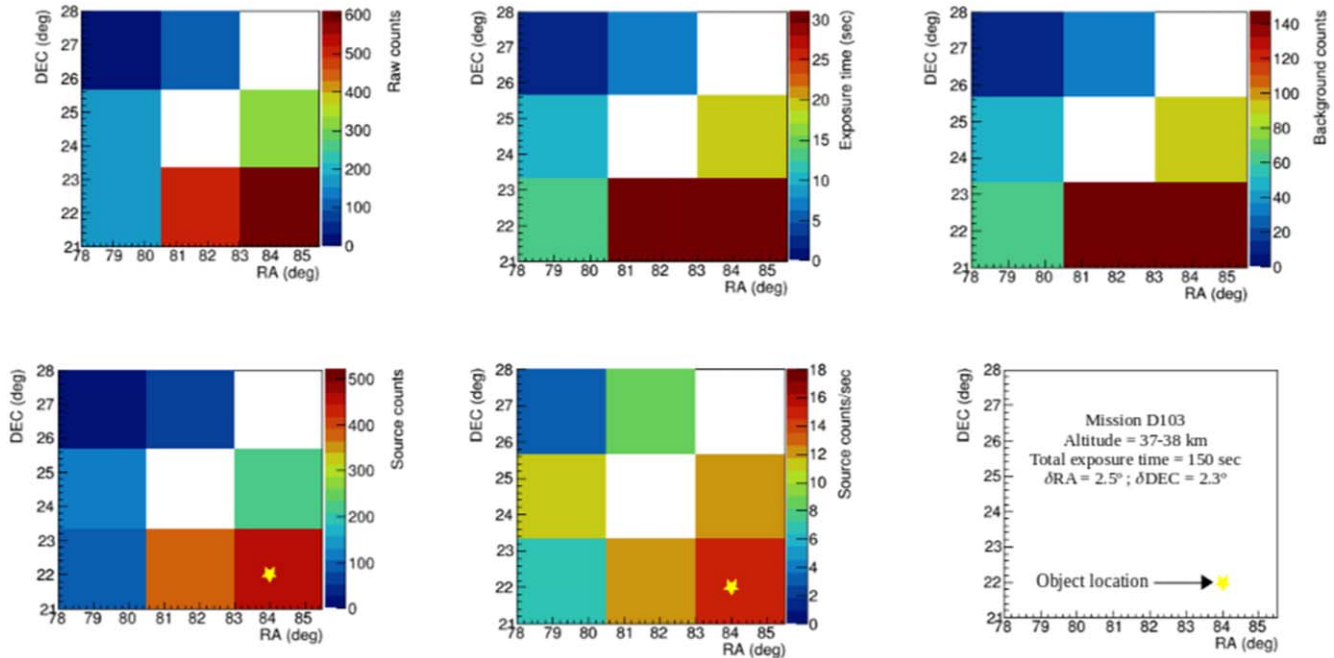


Figure 14. Different stages for the source detection in mission D103. The Crab pulsar is detected at detector altitude of 37 km.

respectively. We also draw the background spectrum for each source. For the background spectrum calculation, we considered a weighted average of the background counts at each atmospheric layer based on the time taken by the payload to pass through each layer. Radiations from astronomical objects

such as the Sun and Crab radiation are detected in D92 and D103, respectively. To obtain low background effects, low atmospheric absorption, high exposure time, and high sensitivity from the detector, we take the highest altitudes. For measuring the spectrum of the Sun in D92, we considered the

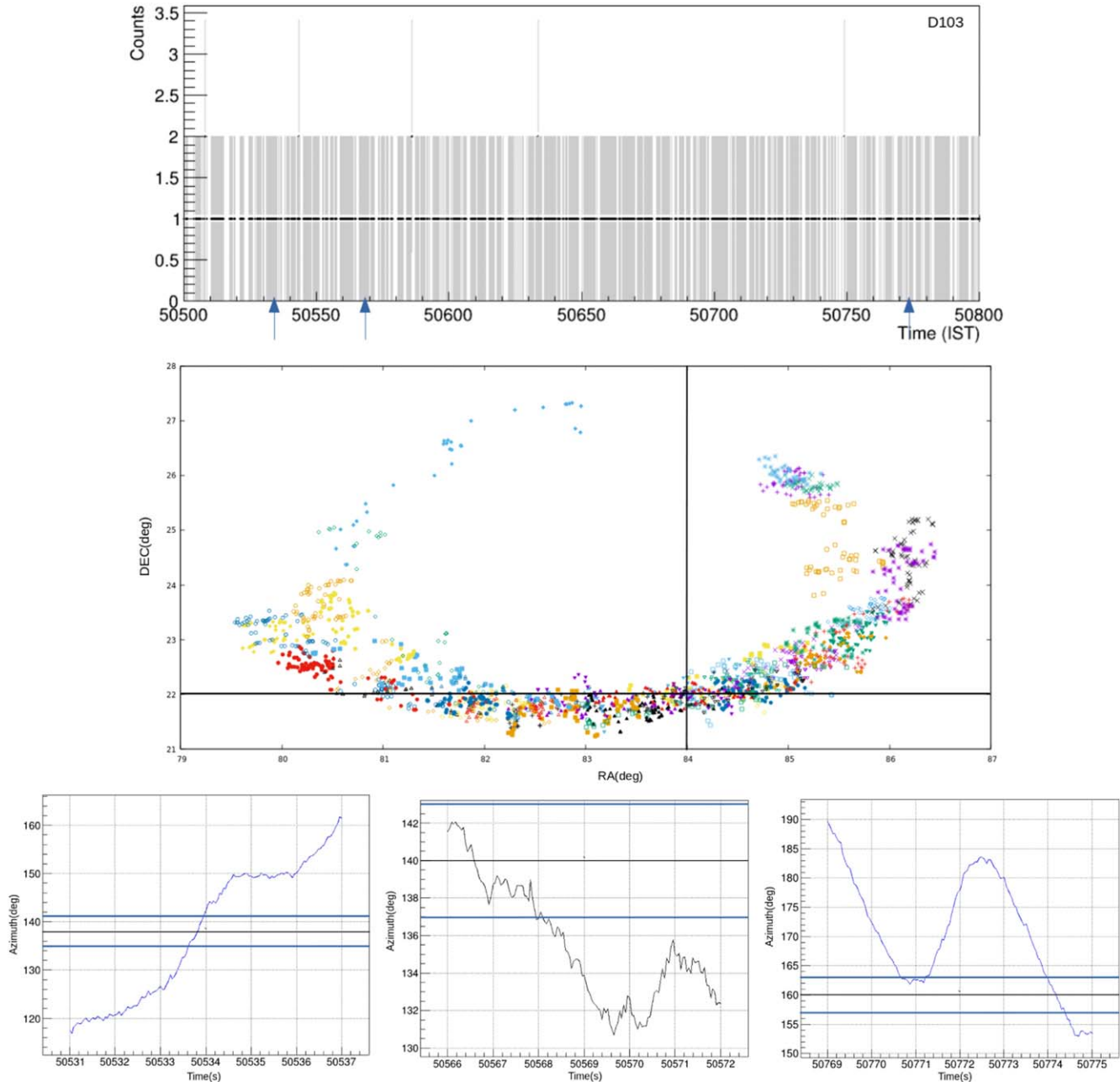


Figure 15. Upper panel: Example of the 1 ms binned Crab data obtained in D103 with time. The blue arrows indicate the six-second chunks used for data analysis due to the reasons present in the text. Middle panel: R.A./decl. plot of all the data from 50,500 to 50,800 s. Different symbols and colors are used to distinguish different 6 s chunks of data. Lower panel: The azimuth plot of three data points (50531–50537) s (left), (50566–50572) s (middle), and (50769–50775) s (right) with time. The angle covered by the blue lines indicates the FOV, and the black lines indicate the azimuthal angle of the Crab.

altitude range of 39–41 km, and for the spectrum of the Crab in D103, we considered the altitude range of 36–39 km. The total exposure time for the Sun’s spectrum is 582 s, and for the Crab’s spectrum, it is 421 s. Using detector responses, atmospheric responses, and background subtraction, we are able to construct the energy spectrum of the strong celestial X-ray sources, the Sun and the Crab pulsar. The detected background plus the

source spectrum along with the calculated background spectrum from our background model without any modifications for the residual atmosphere and the detector response (as an effective area function of the photon energy; Sarkar et al. 2019) are shown on the left side in Figures 17 and 18 for Sun and Crab respectively. After the bin-to-bin subtraction of the background spectrum from background plus source data, we get the source

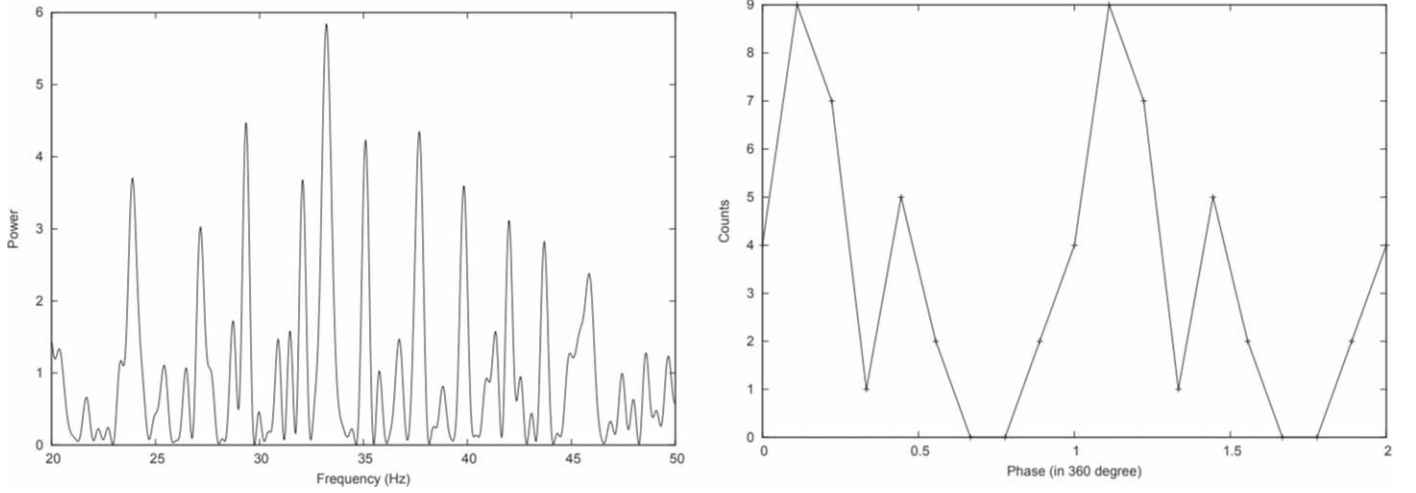


Figure 16. Left: Frequency (Hz) plot of 2 s data from 50,566 to 50,568 s (IST). Right: the phase plot is wrapped around 33.22 Hz relative to the count data, clearly indicating two peaks in the phase range from 0 (0 deg) to 1 (360 deg).

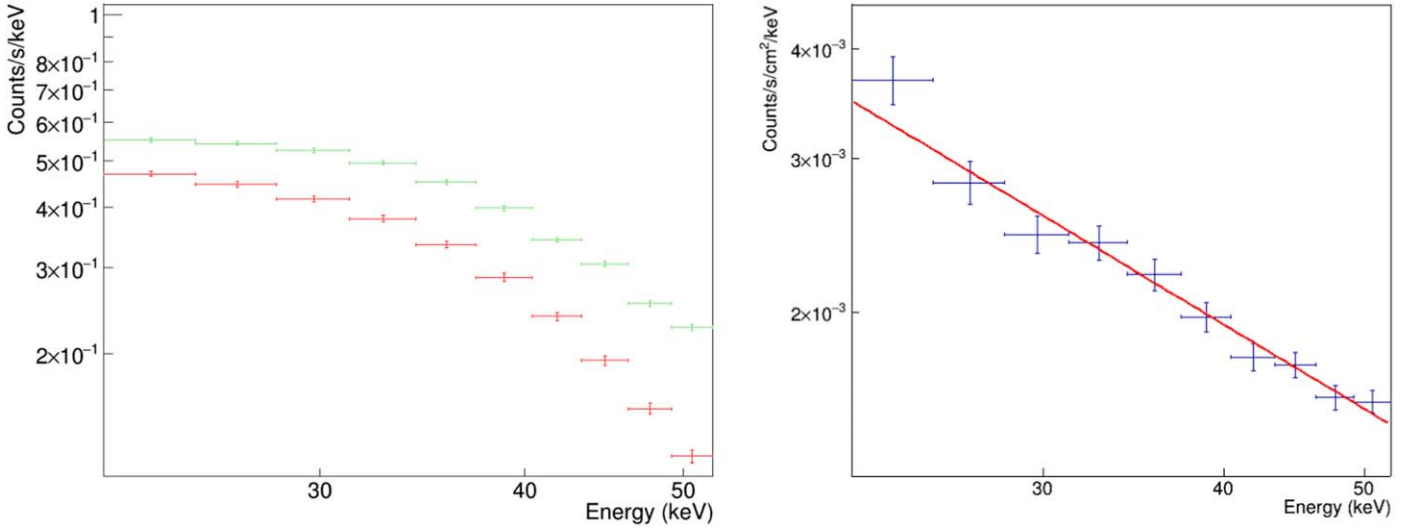


Figure 17. (left) Source plus background spectrum (green) along with calculated background spectrum (red). (right) The Sun's spectrum (blue) is fitted by the power law (red) and modified by the detector and atmospheric responses.

spectrum and further correct it using the atmospheric response and the detector response details in Sarkar et al. (2019). The original spectra of sources thus obtained are fitted by the absorbed power law.

The spectrum of the Sun fitted by the absorbed power-law equation is shown in Figure 17 on the right side. The power law equation (Brown 1971) is given by

$$I_s(E) = C_s E^{-\nu}. \quad (9)$$

In Equation (9), the unit of $I_s(E)$ is $\text{counts s}^{-1} \text{cm}^{-2} \text{keV}^{-1}$. The derived parameters from the best spectral fit in the given energy (E) range are $C_s = (7.64 \pm 1.73) \times 10^{-2} \text{ counts s}^{-1} \text{cm}^{-2} \text{keV}^{-1}$ and $\nu = 9.96 \times 10^{-1} \pm 0.06$, with $\chi^2(8.07)/\text{NDF}(8) = 1.0$. NDF stands for Number of Degrees of Freedom.

The Crab spectrum is fitted by a power law (Kirsch et al. 2005; Sarkar et al. 2019) given by

$$I_c(E) = C_c E^{-\xi} \exp(-0.38\sigma(E)), \quad (10)$$

where $\text{counts s}^{-1} \text{cm}^{-2} \text{keV}^{-1}$ is the unit of $I_c(E)$ and $\sigma(E)$ is the H column photoabsorption cross-section (cm^2) depending on photon energy (E). The Crab spectrum fitted by the absorbed power-law model 10 is shown in Figure 18 on the right side. For the best fit of the Crab spectrum, the values of the two parameters are $C_c = 14.21 \pm 2.02 \text{ counts s}^{-1} \text{cm}^{-2} \text{keV}^{-1}$ and $\xi = 2.56 \pm 0.04$, with $\chi^2 = 19.15$ for $\text{NDF} = 18$.

From the Crab spectrum, we can also calculate the luminosity of the Crab X-ray. The Crab pulsar emission contributes 26% of the total ($\sim 5 \times 10^{38} \text{ erg s}^{-1}$) of its spin-

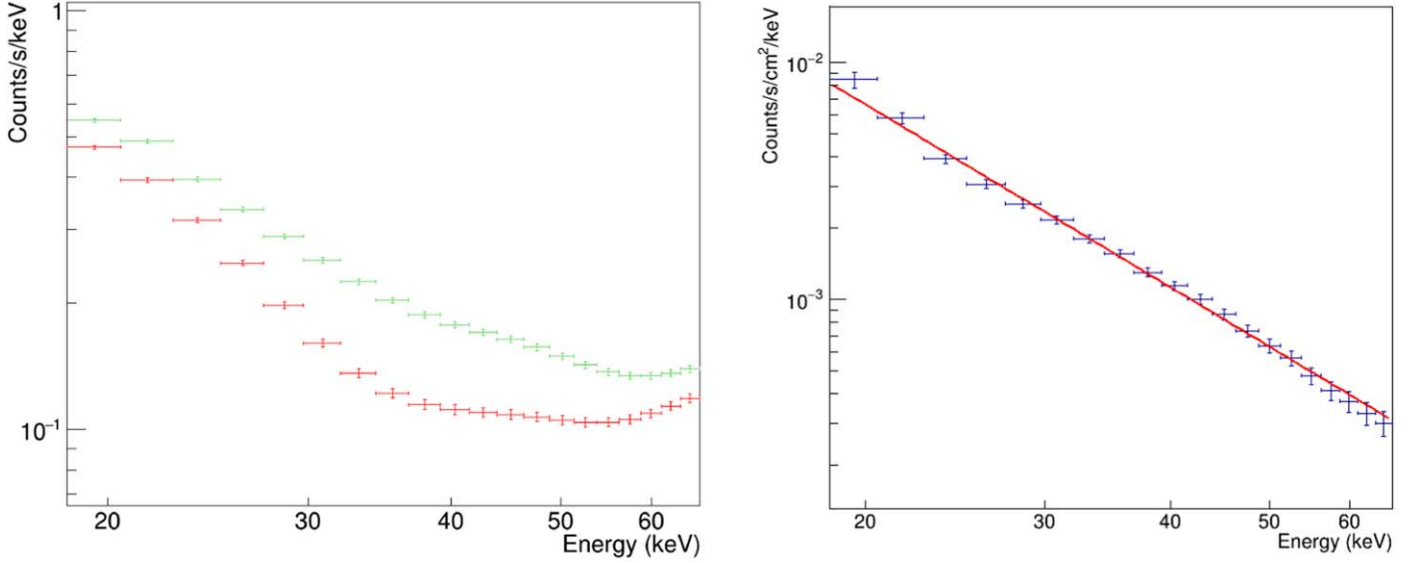


Figure 18. Left: source + background spectrum (green) along with calculated background (red) from the model. Right: the Crab’s spectrum (blue) is fitted by the absorbed power-law model (red) and modified by the detector and atmospheric responses.

down luminosity, which is the integrated luminosity of the value of $\sim 1.3 \times 10^{38} \text{ erg s}^{-1}$ (Hester 2008; Zhang et al. 2022). We have calculated the luminosity of the Crab X-ray using the usual formula $L = 4\pi D^2 f$, where L , D , and f are the luminosity of Crab, the distance of Crab from Earth ($\sim 6500 \text{ ly}$), and the total photon power density of Crab in the photon energy range 20–65 keV evaluated from the integration of the measured Crab spectrum (right side of Figure 18), respectively. The value of f is $\sim 5.67 \times 10^{-5} \text{ erg s}^{-1} \text{ m}^{-2}$. During the calculation of f , we transformed the keV into erg. By putting the values of D ($\sim 61.75 \times 10^{18} \text{ m}$), π , and f in the luminosity formula, we obtained the quantity L with the value of $\sim 3 \times 10^{36} \text{ erg s}^{-1}$, which is much less than the total luminosity and generally agrees with the results presented in the papers Atayan & Aharonian (1996) and Bühler & Blandford (2014) also.

14. Limitations of the Study

Our detectors can detect only photons in the energy range of 1 keV–2 MeV; therefore, higher-energy photons of around GeV (i.e., primary CRs) cannot be detected. Balloon-borne experiments give us a low exposure time for astronomical events or the detection of bright sources because no onboard pointing system is installed. The directional stability of the payload is also low (free rotation of the payload) due to its lightweight nature. No onboard pointing system due to weight restrictions and the height constraint (the highest altitude achieved is $\sim 42 \text{ km}$) of the stratospheric balloon missions would cause some issues with the system’s sensitivity or efficiency to detect astronomical objects or events.

Photons are received at a rate of about one per millisecond and stored on a microSD card using the ARM processor

onboard, and there are an HV DC source of $\sim 700 \text{ V}$ and other instruments such as pre- and post-amplifiers, peak detectors, upper and lower level discriminators, etc. During the mission, the payload is covered by Styrofoam, so the payload is shielded from external thermal variation during the flights. The calibration and energy resolution of the detector before every mission indicate that all instruments are working as expected, and we received high-quality data. The details about the data quality and the extraction process were written and explained in Bhowmick et al. (2019). Using our balloon data, we already showed the CRs to be anticorrelated with solar activity (Sarkar et al. 2017; Sikdar et al. 2023a) during solar cycle 24 and source detection method and timing properties of Crab pulsar (Sikdar et al. 2023c), and we measured the spectrum of solar flares and a gamma-ray burst (Chakrabarti et al. 2014; Sikdar et al. 2023b). Details about data from the balloon missions are presented in Chakrabarti et al. (2017). These data can also be used to observe the geomagnetic storm using 9DOF information at each instant of time.

15. Conclusions

A series of lightweight, low-cost, high-altitude balloon missions have been completed to measure the secondary CRs, to detect several X-ray sources, and to observe occurrences of solar flares, gamma-ray bursts, etc. Our data are also used to obtain atmospheric parameters and radiation from strong astronomical X-ray objects such as the Sun and the Crab. The data also allow us to compute the spectra of such sources. Earlier, we presented some results on the investigation of solar activities, such as the solar flares (Chakrabarti et al. 2017; Sikdar et al. 2023b), the solar winds, etc.

In this paper, we present some important scientific results from our missions, such as the variation of secondary CRs as a function of altitude in the stratosphere, the detection of some astronomical X-ray sources using a unique methodology, and the analysis of the spectra of these sources. Notwithstanding severe limitations (details in Section 14), we achieved remarkable success (Chakrabarti et al. 2017; Sarkar et al. 2020; Sikdar et al. 2023a). The intensity of primary CRs impinging on the top of the atmosphere depends on the geomagnetic field (Störmer 1956), geomagnetic storm (Dorman et al. 1971), solar winds, etc., and the secondary CR is directly dependent on the primary CR. Our result clearly shows how the secondary CR intensity varies with altitude. The detector background comes from many sources. It is mainly due to the secondary CRs (Sarkar et al. 2020) and also due to the internal activities (Gruber et al. 1996) inside the detectors. So, we focus on these issues while obtaining the background calculations. We had to choose a criterion so that the signal (net count minus the background count) to noise ratio is high enough. This is obtained by choosing the appropriate bin size and integrating the photons for a minimum amount of time. After calculation of the R.A., decl., and background subtraction, we could detect the sources, such as the Sun and the Crab pulsar. In fact, our data also showed ~ 33 Hz pulses in Crab (Sikdar et al. 2023c) whenever it was observed. We also determined the luminosity of the Crab X-rays, which is much less than the observed luminosity of approximately 1.3×10^{38} , which is 26% of the total luminosity of the Crab pulsar (Zhang et al. 2022). As said previously, our main instrument is an X-ray detector. After passing the tropopause, the rotational stability of the payload is high with altitude, and after 35 km, it has better stability with respect to lower altitudes because the payload attains an equilibrium position before bursting. That is why we detect strong sources. The sensitivity of the detector after ~ 35 km is high enough to detect such sources (Sarkar et al. 2019) with a low exposure time (for 38–42 km; ~ 1000 s). In the future, we will try to improve the objectives of the missions (increase the payload weight) with onboard pointing systems and instrumentation. With detectors that are able to detect weaker sources with longer exposure, we can get an enhanced signal-to-noise ratio, achieve high stability, calculate in situ background radiation, etc. Using our Dignity balloon data, we will try to observe the geomagnetic storms, solar winds, etc., presented later in another work. We will also use large area solid state detectors. Work is in progress and will be reported elsewhere.

Acknowledgments

The authors would like to thank all the members of the ICSP balloon team, namely, Mr. S. Midya, Mr. H. Roy, Mr. R. C. Das, Mr. U. Sardar, and Mr. R. Sarkar, for their valuable support during the mission operation and data collection. Rupnath Sikdar thanks the University Grants Commission

scholarship, which made this research possible. All data and results are available from the Indian Centre for Space Physics.

References

- Agostinelli, S., Allison, J., Amako, K., et al. 2003, *NuclIn*, 506, 250
 Akeson, R. L., Chen, X., Ciardi, D., et al. 2013, *PASP*, 125, 989
 Atoyan, A. M., & Aharonian, F. A. 1996, *MNRAS*, 278, 525
 Bazilevskaya, G. A., & Svirzhetskaya, A. K. 1998, *SSRv*, 85, 431
 Bhowmick, D., Chakrabarti, S. K., Sarkar, R., Bhattacharya, A., & Rao, A. R. 2019, *JATIS*, 5, 1
 Brown, J. C. 1971, *Solphys*, 18, 489
 Bühler, R., & Blandford, R. 2014, *RPPh*, 77, 066901
 Carlson, P., & Watson, A. A. 2014, *HGSS*, 5, 175
 Chakrabarti, S., Bhowmick, D., Chakraborty, S., et al. 2014, *InJPh*, 88, 333
 Chakrabarti, S., Bhowmick, D., Sarkar, R., Mondal, S., & Sen, A. 2011, *ESASP*, 700, 581
 Chakrabarti, S., Bhowmick, D., Sarkar, R., Bhattacharyya, A., & Midya, S. 2015, *ESASP*, 730, 557
 Chakrabarti, S., Sarkar, R., Bhowmick, D., & Bhattacharya, A. 2017, *ExA*, 43, 311
 Dorman, L. I., Smirnov, V. S., & Tyasto, M. I. 1971, *Cosmic Rays in the Earth's Magnetic Field* (Moscow: Nauka)
 Fittock, M., Siegl, M., Stamminger, A., & Schmidt, A. 2011, Supporting German Rexus Student Experiments to New Heights Onboard Sounding Rockets
 Gaisser, T. K. 1990, *Cosmic Rays and Particle Physics* (Cambridge: Cambridge Univ. Press)
 Grieder, P. K. F. 2001, *Cosmic Rays at Earth: Researcher's Reference, Manual and Data Book* (Amsterdam: Elsevier)
 Gruber, D. E., Blanco, P. R., Heindl, W. A., et al. 1996, *A&AS*, 120, 641
 Harrison, R., Nicoll, K., & Aplin, K. 2014, *JASTP*, 119, 203
 Hester, J. J. 2008, *araa*, 46, 127
 Jain, C., & Paul, B. 2011, *RAA*, 11, 1134
 Kirsch, M. G., Briel, U. G., Burrows, D., et al. 2005, *Proc. SPIE*, 5898, 22
 Mazzeolla, J. M. 2007, *adass*, 376, 153
 Ozyagcilar, T. 2015, Application Note, Rev. 4.0 AN4248, Freescale Semiconductor
 Peterson, L. E., Pelling, R. M., & Matteson, J. L. 1972, *SSRv*, 13, 320
 Phillips, T., Johnson, S., Koske-Phillips, A., et al. 2016, *SpWea*, 14, 697
 Picone, J., Hedin, A., Drob, D., & Aikin, A. 2002, *JGR*, 107, 1468
 Saraiva, J., Blanco, A., & Garzón, J. 2020, *JInst*, 15, C09024
 Sarkar, R., Chakrabarti, S., Bhowmick, D., Bhattacharya, A., & Roy, A. 2019, *ExpA*, 47, 345
 Sarkar, R., Chakrabarti, S. K., Pal, P. S., Bhowmick, D., & Bhattacharya, A. 2017, *AdSpR*, 60, 991
 Sarkar, R., Roy, A., & Chakrabarti, S. K. 2020, *AdSpR*, 65, 189
 Sikdar, R., Chakrabarti, S., & Bhowmick, D. 2023a, *JApA*, 44, 73, 10.1007/s12036-023-09964-6
 Sikdar, R., Chakrabarti, S., & Bhowmick, D. 2023b, *ExpA*, 56, 1
 Sikdar, R., Chakrabarti, S., & Bhowmick, D. 2023c, *MNRAS*, 526, 6181
 Snowman, J., Greig, A., & Richman, D. 2013, Cambridge University Spaceflight Landing Predictor
 Störmer, C. 1956, *QJRMAS*, 82, 115
 Stozhkov, Y., Svirzhetsky, N., & Makhmutov, V. 2002, *Cosmic Ray Measurements in the Atmosphere*
 Tauchid, M., & Grasty, R. L. 2002, *Natural Background Radioactivity of the Earth's Surface—Essential Information for Environmental Impact Studies*
 Thompson, D. J. 1974, *ApJ*, 614, 1113
 Usoskin, I., & Kovaltsov, G. 2006, *JGR*, 111 10.1029/2006JD007150
 Usoskin, I., Schüssler, M., Solanki, S., & Mursula, K. 2005, *JGR*, 110, A10102
 Utomo, Y. 2017, *JPhCS*, 817, 012045
 Wenger, M., Ochsenbein, F., Egret, D., et al. 2000, *A&AS*, 143, 9
 Winckler, J. R. 1961, *RadR*, 14, 521
 Zhang, C.-M., Cui, X.-H., Li, D., et al. 2022, *Universe*, 8, 628
 Zhang, Y., Rossow, W., Laci, A., & Oinas, V. 2004, *JGR*, 109, D19105
 Ziegler, J. 1996, *IBMJ*, 40, 19